NASA Technical Memorandum 83788

The Role of the Reflection Coefficient in Precision Measurement of Ultrasonic Attenuation

Edward R. Generazio
Lewis Research Center
Cleveland, Ohio

Prepared for the
1984 Annual Review of Progress in Quantitative Nondestructive Evaluation
sponsored by the Defense Advanced Research Projects Agency (DARPA)
LaJolla, California, July 8–13, 1984

NASA

ERRATA

NASA Technical Memorandum 83788

THE ROLE OF THE REFLECTION COEFFICIENT IN PRECISION MEASUREMENT OF ULTRASONIC ATTENUATION

Edward R. Generazio

Page 2: Equations (2) and (3) should read as follows:

$$|B_1(f)| = |FS_1(f)|(1 - |R(f)|^2) \exp [-2\Delta x \alpha(f)] \quad (2)$$

$$|B_2(f)| = |FS_1(f)|(1 - |R(f)|^2)|R(f)| \exp [-2(2\Delta x \alpha(f))] \quad (3)$$

THE ROLE OF THE REFLECTION COEFFICIENT IN PRECISION MEASUREMENT OF ULTRASONIC ATTENUATION

Edward R. Generazio
National Aeronautics and Space Administration
Lewis Research Center
Cleveland, Ohio 44135

SUMMARY

Ultrasonic attenuation measurements using contact, pulse-echo techniques are sensitive to surface roughness and couplant thickness variations. This can produce considerable inaccuracies in the measurement of the attenuation coefficient for broadband pulses. Inaccuracies can arise from variations in the reflection coefficient at the buffer-couplant-sample interface. In this paper, the reflection coefficient is examined as a function of the surface roughness and corresponding couplant thickness variations. Interrelations with ultrasonic frequency are illustrated. It is shown that reliable attenuation measurements are obtained only when the frequency dependence of the reflection coefficient is incorporated in signal analysis. Data are given for nickel 200 samples and a silicon nitride ceramic bar having surface roughness variations in the 0.3 to 3.0 μm range for signal bandwidths in the 50 to 100 MHz range.

INTRODUCTION

Ultrasonic evaluation of materials for determining material characteristics such as grain size (refs. 1 to 4), residual stress (refs. 5 to 6), fracture toughness (refs. 7 to 10), and hardness (refs. 11 to 12) is in wide use. Recent experimental and theoretical efforts have been directed toward providing increased accuracy for determining quantitative material characteristics (refs. 13 to 18). Several accepted experimental methods are currently available for determining the ultrasonic attenuation and velocity for solid materials (refs. 19 to 22). These methods have revealed the importance of the relationship between the experimental techniques applied and the experimental results obtained (ref. 21). While the quantitative experimental results should be independent of the method used a substantial amount of variation in the final result is apparent. For example, Papadakis (ref. 21) has described a pulse-echo technique for determining the ultrasonic attenuation and velocity which emphasizes the importance of the experimental technique.

There remains a lack of understanding of the relationship between material microstructure and the data obtained through ultrasonic evaluation. This is partly because of the lack of data and because the data for many experimental systems are subject to rather large errors (refs. 12 and 13, and 15 to 17). Prior experimental systems were typically limited to a narrow range of frequencies for which valid data could be obtained. Systems exhibiting low (high) attenuation require a long (short) sound path lengths in order to obtain reliable data. An experimental problem arises when we attempt to make attenuation measurements (for a sample having fixed dimensions) over a wide frequency range where the attenuation may vary by several orders of magnitude from an extremely high value to an extremely low value. The problem reveals itself in the large

experimental uncertainties at both low and high frequency regimes. It is this experimental constraint coupled with the fairly large experimental errors that has remained one of the major obstacles in the determination of the relationship between material microstructure and the ultrasonic data. This paper provides methodology for determining and verifying the accuracy of attenuation data obtained from ultrasonic pulse-echo techniques.

Data obtained from pulse-echo ultrasonic systems that use a buffer rod are critically dependent on the determination of the buffer rod-couplant-sample (BCS) reflection coefficient in the measurement of ultrasonic attenuation. It is shown here that by correctly determining the (BSC) reflection coefficient reliable attenuation data are obtained. However, reflection coefficients are generally frequency dependent functions that can be shown to be influenced by surface roughness, even roughness down to the micron level.

Surface roughness is also of importance (refs. 23 to 25) for many material samples such as, ceramics and composites where the condition of the surface of the sample can dominate the mechanical test results (refs. 26 and 27) (tensile test, etc.). For ceramics in particular, modification of the surface structure by polishing, etching, etc. is prohibitively costly. Therefore, as a practical matter there are many instances where precise ultrasonic attenuation measurements must be made on a sample having a range of surface roughnesses. It will be shown here that the roughness of the surface of the sample has a significant effect on the reflection coefficient and that this effect is observed in the accuracy of the measured attenuation.

THEORY

The use of pulse-echo techniques are well established. A typical configuration is shown in figure 1(a). A single broad band ultrasonic pulse (main pulse) is excited (via the transducer) in the buffer rod. The ultrasonic pulse is partially reflected at the buffer rod-couplant-sample interface. The first front surface reflected pulse is labeled FS_2 in figure 1(a). When it is not coupled to anything the front surface of the buffer rod reflects back FS_1. The main pulse travels forward through the sample and then reflects off the back surface of the sample and again interacts with the buffer rod-couplant sample interface. This first back surface reflection is labelled B_1'. Echo B_1' is partially reflected at the buffer rod-couplant-sample (BCS) interface and is subsequently reflected again at the back surface. The second back surface reflection is labelled B_2'. Echoes B_1' and B_2' are not directly measurable with the BCS configuration. Their reduced amplitudes, labelled B_1 and B_2 in figure 1(a), are measurable.

The Fourier magnitude of pulses FS_2, B_1, and B_2 are given by:

$$|FS_2(f)| = |FS_1(f)||R(f)| \tag{1}$$

$$|B_1(f)| = |FS_1(f)|(1 - |R(f)|) \exp [-2\Delta x \alpha(f)] \tag{2}$$

$$|B_2(f)| = |FS_1(f)|(1 - |R(f)|)|R(f)| \exp [-2(2\Delta x \alpha(f))] \tag{3}$$

respectively, where $|FS_1(f)|$ is the Fourier magnitude of the first front surface reflection without the sample present on the buffer rod. $|R(f)|$ is the

frequency dependent BCS reflection coefficient and where Δx and $\alpha(f)$ are the thickness of the sample and the frequency dependent attenuation coefficient, respectively.

The attenuation coefficient is obtained by combining equations (1), (2), and (3), and is:

$$\alpha(f) = \frac{1}{2\Delta x} \ln \left\{ \frac{|B_1(f)||R(f)|}{|B_2(f)|} \right\} \tag{4}$$

The theoretical expression for the BCS reflection coefficient is (ref. 28)

$$|R(f)| = \left\{ \frac{\left(1 - \frac{Z_1}{Z_3}\right)^2 \cos^2\left(\frac{2\pi f}{V_2}\delta x\right) + \left(\frac{Z_2}{Z_3} - \frac{Z_1}{Z_2}\right)^2 \sin^2\left(\frac{2\pi f}{V_2}\delta x\right)}{\left(1 + \frac{Z_1}{Z_3}\right)^2 \cos^2\left(\frac{2\pi f}{V_2}\delta x\right) + \left(\frac{Z_2}{Z_3} + \frac{Z_1}{Z_2}\right)^2 \sin^2\left(\frac{2\pi f}{V_2}\delta x\right)} \right\}^{1/2} \tag{5}$$

Here f, V_2 are the frequency and velocity of sound in the couplant layer. Z_1, Z_2 and Z_3 are the acoustical impedance of the buffer rod, couplant, and sample, respectively, and δx is the couplant thickness. At low frequencies and thin couplant thicknesses such as $\delta x/\lambda << 1$ (where λ is the wavelength of sound in the couplant layer) equation (5) reduces to:

$$|R(f)| = \left| \frac{Z_3 - Z_1}{Z_3 + Z_1} \right| \tag{6}$$

and is independent of frequency. Equation (6) has been experimentally verified for systems satisfying the above constraints (ref. 21).

The theoretical reflection coefficient (as determined by eq. (5)) for the experimental arrangement in figure 1 is shown in figure 2. In figure 2 the acoustical impedances used in the calculation are that for a fused quartz buffer rod, nickel 200 metal sample and glycerin couplant. The reflection coefficient is seen to increase with increasing couplant thickness and approaches a constant value of 0.58 for low frequencies. It is emphasized here that the theoretical expressions (eqs. (5) and (6)) are valid for ideally flat and parallel interfaces and for small amplitude waves. Although the small amplitude criteria can usually be met the flatness of the surface of the sample may vary considerably. This is especially true for ceramics (ref. 29) and composite samples where surface topological variations may have dimensions ~1.0 μm. Typically, one expects long wavelength sound (~100 μm) to interact negligibly with thin (thin when compared to the wavelength of sound) barriers. This is theoretically shown in equation (5) for low frequencies (i.e., long wavelength) and thin couplant thickness. For some experimental systems that are topologically rough the long wavelength limit no longer applies and a more detailed examination of the reflection coefficient is required.

For many experimental systems, the validity of the data and data analysis is generally determined by reproducibility of the data and error analysis.

Fortuitously the validity of the attenuation measurement can be verified by using the BCS reflection coefficient and the observed attenuation to predict the waveshape and/or the frequency spectra of the later occurring echoes. The Fourier magnitude of the n^{th} back reflected echo is given by:

$$|B_n(f)| = |B_1(f)||R(f)|^{(n-1)} \exp(-2\Delta x \alpha(f)(n-1)) \quad (7)$$

where n is an integer number ($n \geq 1$) equal to the number of back surface reflections the n^{th} pulse has undergone and $|B_n(f)|$ is the Fourier magnitude of the n^{th} pulse.

EXPERIMENT

There are three parts to this investigation in which the ultrasonic attenuation is measured for metallic and ceramic samples. The experimental configuration is shown in figures 1 and 3. A broadband transducer having a center frequency of 50 MHz is excited with a drive pulse from the pulser-receiver. Typical received echoes are shown in figure 1(b). In figure 1(b) the front surface reflection FS_2, first back surface echo B_1, second back surface echo, B_2, and third back surface echo B_3, are shown. During data acquisition, each echo shown in figure 1(b) and the front surface reflection, FS_1 (not shown) is individually windowed using the digital time delay and digitized into a 512 element array. Each signal is Fourier transformed, into the frequency domain using a digital Real Fast Fourier Transform (RFFT) algorithm included in the computer software.

The reflection coefficient of the BCS system is determined from the front surface reflections FS_2 and FS_1 that are obtained with and without the sample in place, respectively, and by use of equation (1). Care must be taken to ensure that a valid echo FS_2 arises when a sample is coupled to the buffer rod. The couplant must be free of bubbles after sample is coupled to the buffer rod. The pressure on the sample is increased until no further change is observed in the amplitude of echo FS_2. This can be accomplished reproducibly.

A metal sample is used in the first part of this investigation. The metal sample is Nickel 200 and has dimensions of 1.9 by 1.9 by (0.2540 $\pm$ 0.0003) cm thick. The sample was produced from stock Ni 200 that has been cold rolled 50 percent annealed at (1250 $\pm$ 15° F) for 15 min, then cold rolled 50 percent. Both sides of the sample are polished to a "mirror" finish with the final polishing being done with a slurry containing 1.0 μm diameter aluminum oxide.

The nickel sample was roughened on one side (the interface side) by polishing in successive steps with 3.0 μm diamond grit paste and with silicon carbide grinding papers containing particles having mean (nominal) dimensions of 15, 23, 30, 35, and 70 μ. After each roughening step the topology of the roughened surface was measured with a profilometer. The reflection coefficient and the attenuation are also measured after each roughening step.

A ceramic sample is used in the second part of this investigation. The ceramic sample is an as-ground fully dense Si_3N_4 ceramic MOR bar. The surface profile, ultrasonic reflection and attenuation coefficients were measured.

Lastly, an ordered array of etched pits are produced on the surface of a nickel sample. The scatters (etched pits) on this nickel sample were produced by a photolithographic technique. The surface profile, reflection, and attenuation coefficients were measured for this sample before and after etching.

Surface Profiles

The surface profiles for the roughened nickel sample (shown in fig. 4) reveals the roughness of the surface of the sample after being roughened with 1.0, 3.0, 15, 23, 30, 35, and 70 μ diameter grits. The magnitude of the topological variations generally increases with increasing diameter polishing grips except for the case where the polishing compound is 3.0 μm diameter diamond grit. In this case, the greater roughness is attributed to selective cutting by the diamond particles.

The surface profile of the as-ground Si_3N_4 ceramic MOR bar is shown in figure 5. The topological variations are quite large at about 2.5 μm.

The ordered set of scatterers produced on the nickel sample is an array of 1.2 μm deep etched pits having lateral dimensions of ~49 μm by ~62 μm. These etched pits are shown as the dark areas in figures 6(a) and (b). Figure 6(c) shows the surface topology of this sample.

Reflection Coefficient

The reflection coefficient as a function of frequency for each successive surface roughness condition of the polished nickel sample is shown in figure 7. Each curve is labeled according to the polishing grit size (in microns) used to roughen the surface of the sample. The increase in the reflection coefficient below 30 MHz is due to a minimum in the magnitude of the frequency spectra $|FS_1(f)|$. At this minimum the ratio of the frequency spectras, used to determine the reflection coefficient, is subject to large errors. Similarly, there is a sharp decline in the reflection coefficient above 75 MHz where a minimum in the magnitude spectra $|FS_2(f)|$ is observed. These minima lead to large errors in the determination of the reflection coefficient, therefore, we define a valid zone from 30 to 75 MHz, outside this zone the data are questionable. Figure 8 shows the reflection coefficient as a function of the peak-to-valley surface roughness as determined from figures 4 and 7. Note that, the reflection coefficient (at a fixed frequency) is not a monotonically increasing function of the surface roughness.

The reflection coefficient as a function of frequency for the ceramic sample is shown (solid curve) in figure 9. The reflection coefficient given by equation (6) is also shown as a dashed line. The shaded regions indicate that the data in these regimes is of questionable validity.

The front surface reflection FS_2 is shown in figures 10(b) and (c) for the unetched and etched array sample configuration, respectively. Here, the front surface reflection FS_1, shown in figure 10(a) is identical for both configurations since it comes from the buffer rod before coupling. The reflection coefficient for both configurations is shown in figure 10(d). Here, the dashed curve and solid curve are for the etched and unetched configurations, respectively. The reflection coefficient for the unetched systems is smooth (in the

region of validity 30 to 75 MHz) and similar to that shown previously. The etched pit system exhibits a fluctuating reflection coefficient over the same frequency range.

If we subtract the front surface reflection FS_2 for the unetched system from the front surface reflection FS_2 for the etched system we obtain a residual reflected waveform (shown in fig. 10(e)) which is approximately due to the interaction of the main pulse with the individual etched pits and nickel protrusions (light areas in fig. 6(a)). This subtraction process is an approximation in that an exact result requires knowledge of the couplant thickness for each of the two cases. The residual reflected waveform has a similar shape to that of a damped resonance (ref. 30).

Attenuation Coefficients

Attenuation measurements were made using procedures described above and by use of equations (1) to (4). A diffraction correction (refs. 21, 31 and 32) has not been included in the following data analysis. This correction is negligible (less than 0.01 Np) above 25 MHz for the nickel sample.

In figure 11(a), the attenuation for all surface roughnesses is shown and has been calculated according to equation (4) where the reflection coefficient is determined by use of equation (1). There exists a random error in the attenuation results. At 30, 50, and 65 MHz the experimental uncertainties in the measurement of the attenuation are 0.09, 0.17 and 0.4 Np/cm, respectively. In figure 11(b) the attenuation for all surface roughness is shown for the case where the reflection coefficient (as given by use of eq. (6)) is considered to be independent of frequency. At 30, 50, and 65 MHz the experimental uncertainties in the measurement of the attenuation are 0.17, 0.25, and 0.58 Np/cm, respectively. The measured atenuation should be independent of the surface condition (i.e., the BCS reflection coefficient) of the sample being investigated. The data indicates that attenuation measurements that made use of the frequency dependent reflection coefficient are more accurate over the valid frequency range.

The attenuation for the ceramic sample is shown in figure 12. The observed attenuation coefficient is quite low at about 0.5 Np/cm at 100 MHz. When the frequency independent reflection coefficient is used in the determination of the attenuation, the resulting attenuation coefficient is negative (shown as a dotted line in fig. 12) and represents a gain in signal amplitude. This is clearly contradictory because it implies spontaneous signal amplification by the sample.

The attenuation for the unetched and etched array configuration is shown in figure 13. The solid and dotted curve refer to the unetched and etched systems, respectively. The attenuation for the etched system is found to be oscillatory and less than or equal to the attenuation for the unetched system. Here the frequency dependent reflection coefficients shown in figure 10(d) are used in the determination of the attenuation.

Predicted Results

The predicted and observed waveform and frequency spectra of echo B_3 for the nickel sample roughened with 35 μm silicon carbide are shown in figure 14. The dotted curves in figure 14 refer to the predicted results and the solid curves refer to the experimental measured values for pulse B_3. The predicted results differ from the experimental results within ~1 percent in the range of frequencies 30 to 65 MHz. These data indicate that an accurate attenuation measurement has been made.

The predicted frequency spectrum for pulse B_3 for the ceramic sample is shown in figure 15 (dotted curve) along with the observed frequency spectrum (solid curve) of pulse B_3. At 100 MHz the two spectra differ by about 14 percent. Although this error is large, it is to be expected for a system having a high reflection coefficient and low attenuation typical for ceramics coupled to a quartz buffer, as in this case.

For systems with a high reflection coefficient only a small amount of energy of the main pulse FS_1 enters the sample and similarly only a small amount of energy is allowed to leave the sample for each of the back scattered pulses, B_1, B_2, and B_3. Therefore, the signal to noise ratios for these pulses B_1, B_2, and B_3 are quite low. The use of these noisy pulses result in large errors in the attenuation measurements. A discussion of the origin of intrinsic errors that are introduced into the reliability of the data is presented in the Appendix.

DISCUSSION

The reflection coefficients shown in figure 7 are observed to vary considerably as the roughness of the surface is increased. For the system roughened with 35 μm grit the reflection coefficient is found to vary up to ~9 percent of its value at 30 MHz. This is consistent with equation (5) if it is assumed that an increase in surface roughness leads to an effective increase in the couplant thickness δx. The mean increase couplant thickness due to roughness is shown in figure 16. Here, the sample surface is that for the 35 μm case. It is expected that the couplant fills in the cavities existing on the surface of the sample and that these filled cavities lead to an effective increase in the local couplant thickness.

The reflection coefficient shown in figure 8 (at a fixed frequency) is not a monotonically increasing function of the surface roughness. This appears to contradict equation (5) and figure 2 where an increase in couplant thickness results in an increase in the reflection coefficient (for fixed frequency). It is likely that an increase in surface roughness corresponds to an increase in the surface area of the sample that is in direct physical contact with the buffer rod. Further, an increase in the "contact" area between the sample and the buffer rod will be represented as a decrease in the reflection coefficient. Therefore, for any experimental configuration we must consider not only the effective changes in the couplant thickness due to surface roughness but also changes in the "contact" area between the sample and surface (ref. 33). This is a formidable problem in that the topology of the surface of the sample must be known in detail everywhere and is beyond the scope of the present work. It is also likely that the uncertainty of the pressure applied to the sample may lead to the nonmonotonic reflection coefficient data shown in figure 8.

The trend of increasing reflection coefficient with increasing surface roughness is reproducible for the roughened Nickel 200 sample. This indicates that, for the surface roughnesses and the frequency range investigated, the use of the frequency dependent reflection coefficient (eq. (5)) in the calculation of the attenuation coefficient yields (eq. (4)) yields more reliable data than the use of the frequency independent reflection coefficient (eq. (6)) in the same measurement. This is dramatically shown for the ceramic sample where the use of the frequency independent reflection coefficient in the calculation of the attenuation coefficient yields completely erroneous results (see fig. 12).

The experimentally measured reflection coefficients shown in figures 7 and 9 are qualitatively similar to theoretical reflection coefficient shown in figure 2. This suggests that the effective couplant thickness for a rough surface is larger than that for a "smooth" surface.

The random topological variations (roughness) existing on the surface of a sample are likely to scatter energy out of the main pulse in a random manner. Consequently the loss of this randomly scattered energy will result in a reduced amplitude for reflection FS_2 so that the reflection coefficient calculated from equation (1) is expected to have a somewhat lower value than that for ideally flat surfaces.

The accuracy of our attenuation data was verified by accurately predicting the amplitude of the third reflection, B_3 for the Nickel 200 sample. This indicates that the above-mentioned scattered energy is small. However, this energy may be scattered by the topological (roughness) sites, to form a series of nearly in phase Huygen wavelets (refs. 34 and 35). These nearly in phase spherical waves act together to form a second plane wavefront so that the reflection FS_2 is constructed of two wave components: a component due to the increased couplant thickness and a component due to the scattering sites existing on the surface of the sample. The presence of both of these mechanisms will result in a reflection coefficient that is higher than expected for an ideally flat surface.

Data obtained for the metal sample having an ordered set of scatters (see fig. 10) support the possibility of the coexistence of these two mechanisms. Here the presence of ringdown in the reflection pulse FS_2 (shown in fig. 10(c)) and the identification of a residual reflected wave (shown in fig. 10(e)) are indications that the presence of surface roughness (~1.2 μm) does indeed scatter the main pulse FS_1 (see fig. 15(a)) into a reflected pulse FS_2 (see fig. 10(c)) made up of at least two components. The subtracted pulse (see fig. 10(b)) representing the reflected wave due to the couplant thickness and a scattered wave (i.e., the residual wave shown in fig. 10(e)) due to the ordered array of scatters. The actual scattering mechanism remains unknown but is likely to be due to mode conversion (ref. 36). It is clear that substantial scattering of the main pulse, FS_1 has occurred and that this scattering is due to the ordered surface roughness of the sample.

It has been found that the use of the frequency dependent reflection coefficient in the measurement of attenuation yields more accurate results than the use of the frequency independent reflection coefficient in the same measurement. This is <u>valid</u> for experimental samples having <u>randomly rough</u> surfaces at least in the range from 0.05 to 2.25 μm investigated here. Experimental samples having excessively rough surfaces result in high reflection coefficients. Further, a high reflection coefficient in the measurement of attenuation results in a decrease in the accuracy of the calculated results. It has

been shown that for an experimental sample having an ordered set of scatters on the surface an erroneous attenuation measurement will be obtained.

Since most experimental samples have some degree of roughness, (i.e., they are not ideally flat) it seems likely that some of the energy of the main pulse is lost via random scattering. Further, if the topology of the sample is ordered then systematic scattering of the main pulse may lead to an attenuation measurement that is of questionable validity. This suggests that further investigation of systems having ordered surface structure is needed.

CONCLUSION

We have shown that accurate measurement of ultrasonic attenuation depends on determining the frequency dependence of the reflection coefficient at the transducer-sample interface. The surface roughness of experimental samples was shown to have a dramatic effect on both the effective couplant thickness and the waveshape of an acoustic pulse reflected at the (transducer) buffer rod-couplant-sample interface. We found that accurate attenuation measurements could be made with randomly rough surfaces.

However, the attenuation measurements will be erroneous if an ordered set of scatters exist on the surface. In the later case we found a two-component pulse reflected at the buffer rod-couplant-sample interface. The presence of this two-component reflected pulse resulted in an erroneous attenuation measurement. Our results demonstrate the importance of surface structure on attenuation measurements and indicate an appropriate procedure for accounting for random surface roughness by measuring the frequency dependence of the reflection coefficient.

APPENDIX

The rather large reflection coefficient for the ceramic sample has affected the precision of the attenuation measurement. This large reflection coefficient is an indication that only a small amount of the main pulse's energy (energy of pulse FS_1) has been transmitted into the ceramic sample. Additionally, this small amount of energy once in the sample tends to remain within the sample. Hence, the signal-to-noise ratios of pulses B_1 and B_2 are quite small. Similarly, for a system having a low reflection coefficient, the signal-to-noise ratios of FS_2 and B_2 are small. Between these extreme cases of low or high reflection coefficients there exists a regime where the S/N ratio is high and the amount of error in the acquired signals is low.

The error introduced into the attenuation measurement due to the low amplitudes of the observed signals may be determined from equations (1) to (4) and the variance relation (ref. 37):

$$\sigma_\alpha^2 = \left(\frac{\partial\alpha}{\partial B_1}\right)^2 \sigma_{B_1}^2 + \left(\frac{\partial\alpha}{\partial B_2}\right)^2 \sigma_{B_2}^2 + \left(\frac{\partial\alpha}{\partial FS_1}\right)^2 \sigma_{FS_1}^2 + \left(\frac{\partial\alpha}{\partial FS_2}\right)^2 \sigma_{FS_2}^2 \tag{8}$$

where σ_α^2, $\sigma_{B_1}^2$, $\sigma_{B_2}^2$, $\sigma_{FS_1}^2$ and $\sigma_{FS_2}^2$ are the variances of the attenuation coefficient, α, and pulses B_1, B_2, FS_1 and FS_2, respectively. By assuming that the variances are the same for all the pulses concerned (usually observed experimentally) we have:

$$\sigma_n^2 = \sigma_{B_1}^2 = \sigma_{B_2}^2 = \sigma_{FS_1}^2 = \sigma_{FS_2}^2 \tag{9}$$

where σ_n is noise variance. By combining equation (8) with equations (1) to (4) we obtain the relation:

$$\left|\frac{\sigma_\alpha}{\alpha}\right| \left(\frac{S}{N}\right) = \frac{1}{2\Delta x\alpha} \left\{ \left[\frac{\left(\exp\left(2\Delta x\alpha\right) + |R|^2\right) \exp\left(2\Delta x\alpha\right)}{\left(1 - |R|^2\right)^2} + 1 \right] \frac{1}{|R|^2} + 1 \right\}^{1/2} \tag{10}$$

where

$$\frac{S}{N} \approx \frac{FS_1}{\sigma_{FS_1}} \tag{11}$$

is the signal to noise ratio of the main pulse FS_1.

The interrelation given by equation (10) is plotted in figure 17. The term $2\alpha\Delta x$ represents the total energy lost (via attenuation) during one round trip through the sample. A minimum in the variance σ_α occurs at $R = 0.58$ for the values of $2\alpha\Delta x$ shown here. The magnitude of the variance σ_α, for fixed $2\alpha\Delta x$ are asymmetric with respect to the reflection coefficient about their minimum values occurring at $R = 0.58$ and this asymmetry indicates that a lower value than $R = 0.58$ is preferred over a value higher than $R = 0.58$.

Where $R = 0.58$ is the optimum reflection coefficient that will result in the least error in the attenuation measurement due to the uncertainty in the pulse amplitudes. This is a universal result for all systems that use the pulse echo method described here. The two shaded trajectories in figure 17 indicate approximately the variance $|\sigma_\alpha/\alpha|$ (S/N) for the roughened Nickel 200 and ceramic data. The longer shaded path originating at $R = 0.58$ is that for the nickel sample and the shorter path originating at $R = 0.7$ is that for the ceramic sample. The absolute value of the variance for both the metal and ceramic sample are shown in figure 18(a). Although the variance for the ceramic attenuation data where is generally less than that for the Nickel 200 attenuation data, the actual percent error given by:

$$\left|\frac{\sigma_\alpha}{\alpha}\right| \times 100 \text{ percent} \qquad (12)$$

for the ceramic sample is greater than that for the metal sample. This is shown in figure 18(b). The percent error results shown in figure 18(b) are consistent with the spread in the attenuation data. The predicted pulses B_3 for both the ceramic and metal sample are also with their respective percent errors. In general, the equation (10) must be numerically solved using the measured values of $2\Delta x\alpha(f)$ and the reflection coefficient $|R(f)|$ in order to determine the trajectories of the variance for a particular data set.

REFERENCES

1. Papadakis, E. P., J. Appl. Phys., 35, 1588 (1964).
2. Papadakis, E. P., Met. Trans., 1, 1053 (1970).
3. Papadakis, E. P., J. Acoust., Soc. 37, 711 (1965).
4. Papadakis, E. P., J. Acoust., Soc. 43, 876 (1968).
5. Allen, D. R., Cooper, W. H. B., Sayers, C. M., and Silk, M. G., Research Techniques in Non-destructive Testing, Academic Press, Chapter 4 (1983).
6. Emery, A. F., Thomas, G. H., and Goods, S. H., ASME-Pressure Vessels + Piping Conference Paper, 83, PVP-31 (1983).
7. Vary, A., and Hull, D. R., Fourteenth Symposium on Non-destructive Evaluation (1983).
8. Vary, A., Fracture Mechanics, ASTM-STP-677 (1979).
9. Vary, A., and Hull, D. R., Materials Evaluation, 41, 309 (1983).
10. Vary, A., Mechanics of Non-destructive Testing, Plenum Press, 123 (1980).
11. Armstrong, R. W., and Jindal, P. C., Trans. TMS-AIME, 242, 2513 (1968).
12. Papadakis, E. P., J. Acoust. Soc. Am., 32, 1628 (1960).
13. Evans, A. G., Kino, G. S., Khuri-Yakub, P. T., and Tittmann, B. R., Materials Evaluation, 35, 85 (1977).
14. Smith, R. L., Rusbrudge, K. L., Reynolds, W. N., and Hudson, B., Materials Evaluation, 41, 219 (1983).
15. Smith, R. L., Reynolds, W. N., Wadley, H. N. G., Metal Science, 15, 554 (1981).
16. Klinman, R., Webster, G. R., Marsh, F. J., and Stephenson, E. T., Materials Evaluation, 38, 26 (1980).
17. Smith, R. L., and Reynolds, W. N., J. Mat. Sci., 17, 1420 (1982).
18. Papadakis, E. P., J. Acoust. Soc. Am., 70, 782 (1981).
19. Papadakis, E. P., Critical Reviews in Solid State Sciences, CRC-373 (1973).
20. Papadakis, E. P., and Fowler, K. A., J. Acoust. Soc. Am., 50, 729 (1971).
21. Papadakis, E. P., and Fowler, K. A., J. Acoust. Soc. Am., 53, 1336 (1973).
22. Papadakis, E. P., J. Acoust. Soc. Am., 44, 1440 (1968).
23. Quentin, G., deBilly, M., Cohen, T. F., Doucet, J., and Jungman, A., IEEE Ultrasonic Symposium Proceedings, 102 (1975).
24. Eitzen, P. G. and Blessing, G. V., May, 21-24, ASNT Spring Conference 1984, Denver, CO, to be published.
25. Haines, N. F., and Langston, D. B., J. Acoust. Soc. Am., 67,, 1443 (1980).
26. Sedlacek, R., Halden, F. A., Jorgensen, P. J., NBS Special Publication 348, 89 (1972).
27. Noone, M. J., Heuer, A. H., NBS Special Publication 348, 213 (1972).
28. Kinsler, L. E., Frey, A. R., Coppens, A. B., and Sanders, J. V., Fundamentals of Acoustics, 3rd ed., John Wiley a Sons, Chapter 6 (1982).
29. Messing, L. G., McCoy and Hassler, C. T., NBS Special Publication 562, 247 (1979).
30. Andronov, A. A., Vitt, A. A., and Khaikin, S. E., Theory of Oscillators, Pergamon Press, Ltd., Chapter I (1966).
31. Papadakis, E. P., J. Acoust, Soc. Am., 52, 847 (1972).
32. Seki, H., Granato, A., Truell, R., J. Acoust. Soc. Am., 28 (1956).
33. Alers, G. S., and Graham, L. J., IEEE Ultrasonic Symposium Proceedings, 579 (1975).
34. Jenkins, A. F., and White, H. E., Fundamentals of Physical Optics, 1st ed., McGraw-Hill Book Company, Chapter 3 (1937).
35. Stephens, R. W. B., and Bate, A. E., Acoustics and Vibrational Physics, 2nd ed., William Clowes and Sons, Chapter 6 (1966).

36. Ko, R., Adler, L., Roberts, R., Achenbach, J., Jungman, A., Quentin, G., "Review of Progress in Quantitative Nondestructive Evaluation," 3B (1984).
37. Bevinton, R. P., Data Reduction and Error Analysis for the Physical Sciences, McGraw-Hill, Chapter Four (1969).

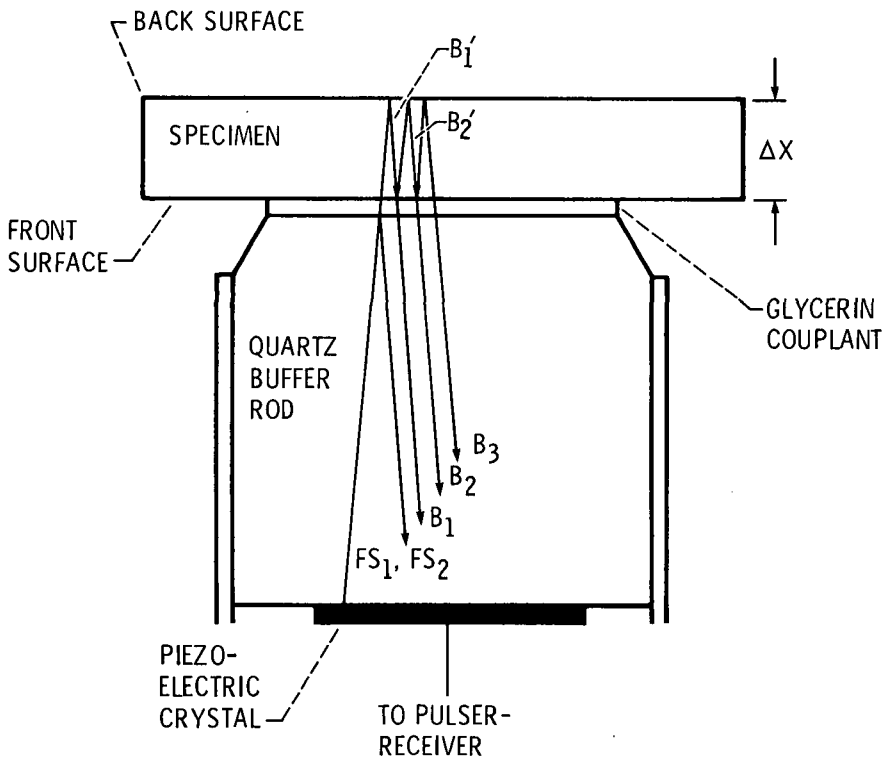

(a) Transducer configuration. Reflected pulses FS_1 and FS_2 are front surface reflections without and with the sample present, respectively.

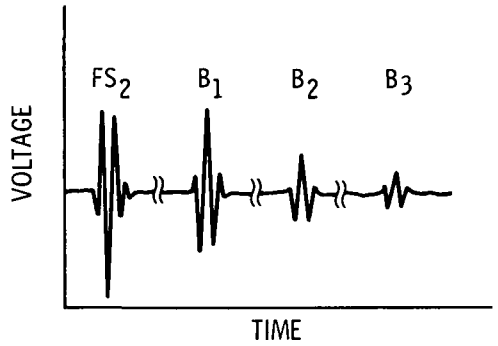

(b) Shown are typical waveforms of echoes FS_2, B_1, B_2 and B_3.

Figure 1. - Specimen/transducer configuration for pulse echo ultrasonic measurements.

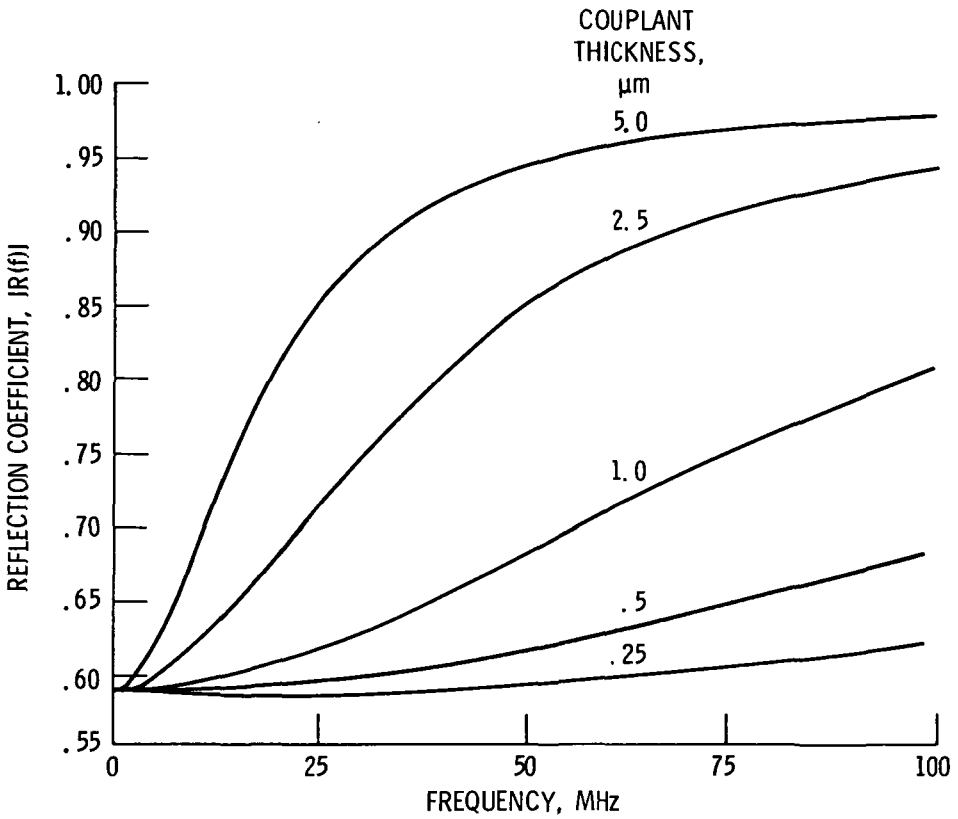

Figure 2. - Theoretical reflection coefficient for varying couplant thickness. The theoretical reflection coefficient determined by use of equation (5) for the configuration shown in figure 1(a) for a nickel 200 sample, glycerin couplant and quartz buffer rod. The numbers on the figure refer to the glycerin couplant thickness in microns.

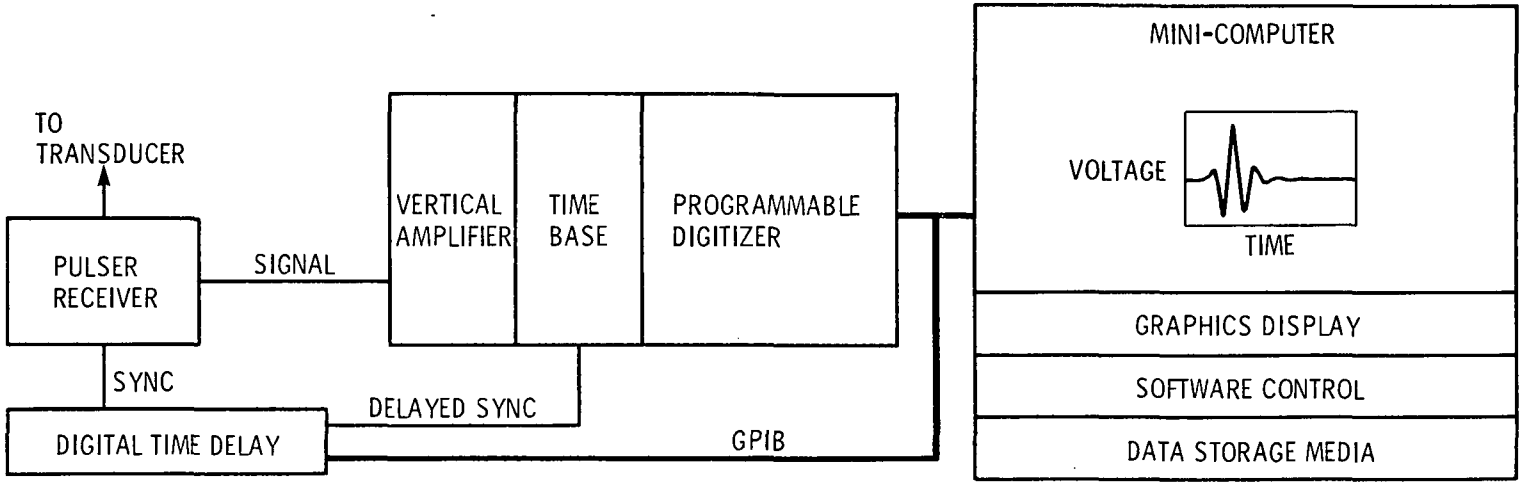

Figure 3. - Block diagram of components used for ultrasonic data aquisition.

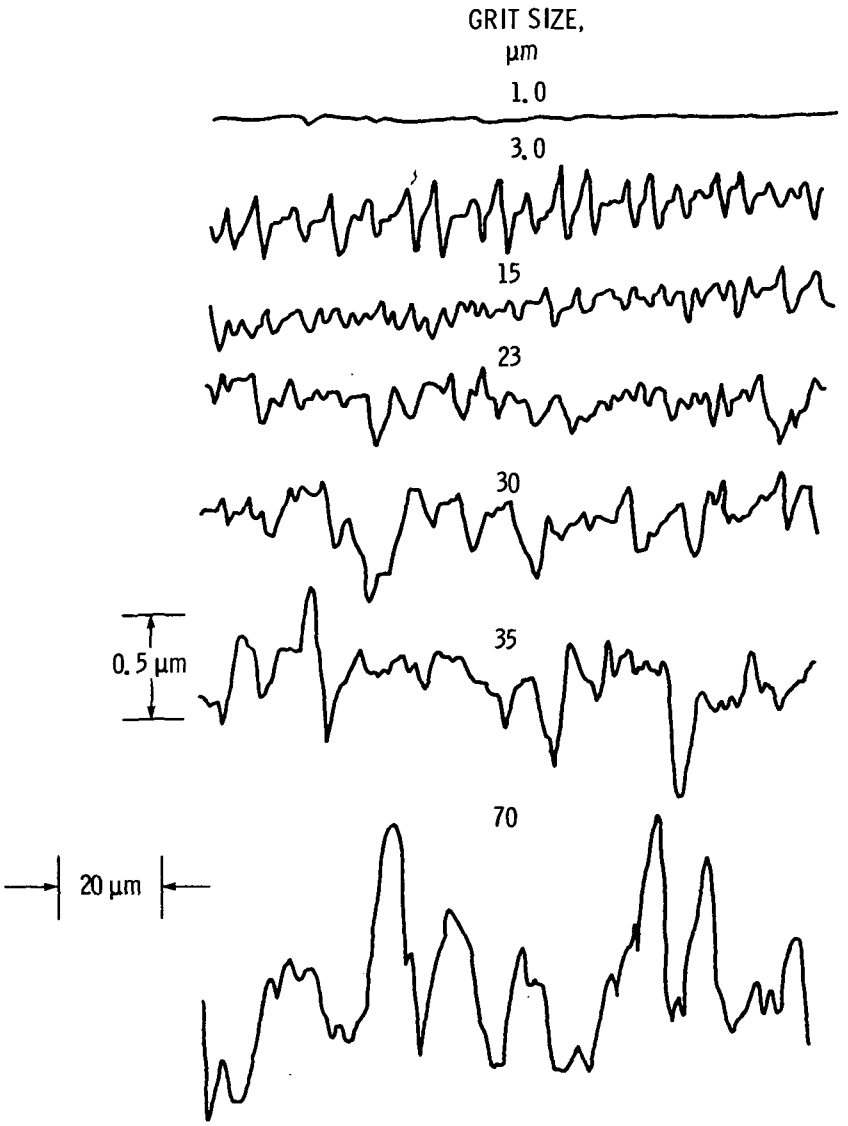

Figure 4. - Representative surface profiles of nickel 200 sample roughened with 1.0 μm aluminum oxide, 3.0 μm diamond grit, 15, 23, 30, 35, and 70 μm silicon carbide grit. Roughness measured by profilimiter.

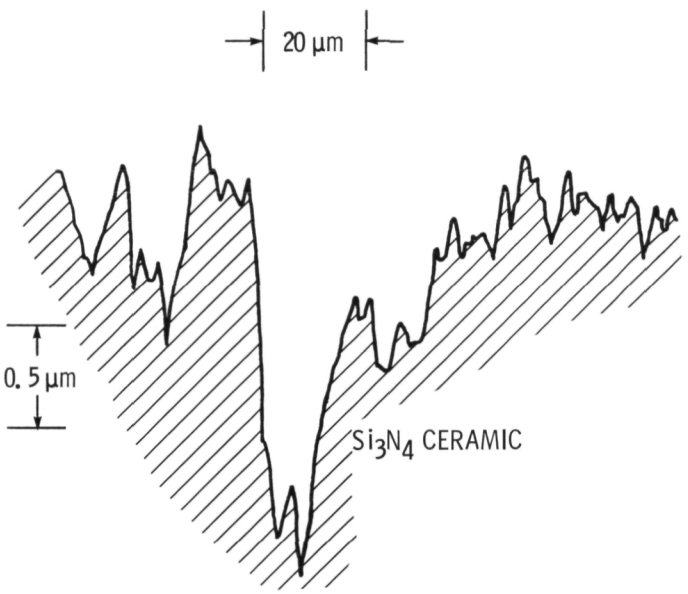

Figure 5. - Representative surface profile of as-ground Si_3N_4 ceramic MOR bar.

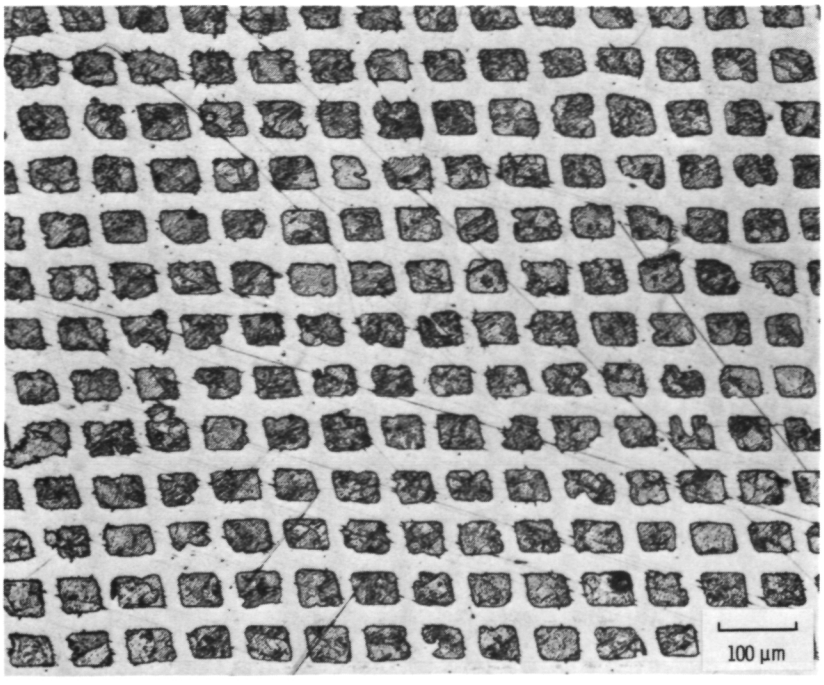

(a) Top view of the array of pits etched into the nickel 200 sample. The dark areas represent the bottom of the pits and the light areas represent the surface of the sample.

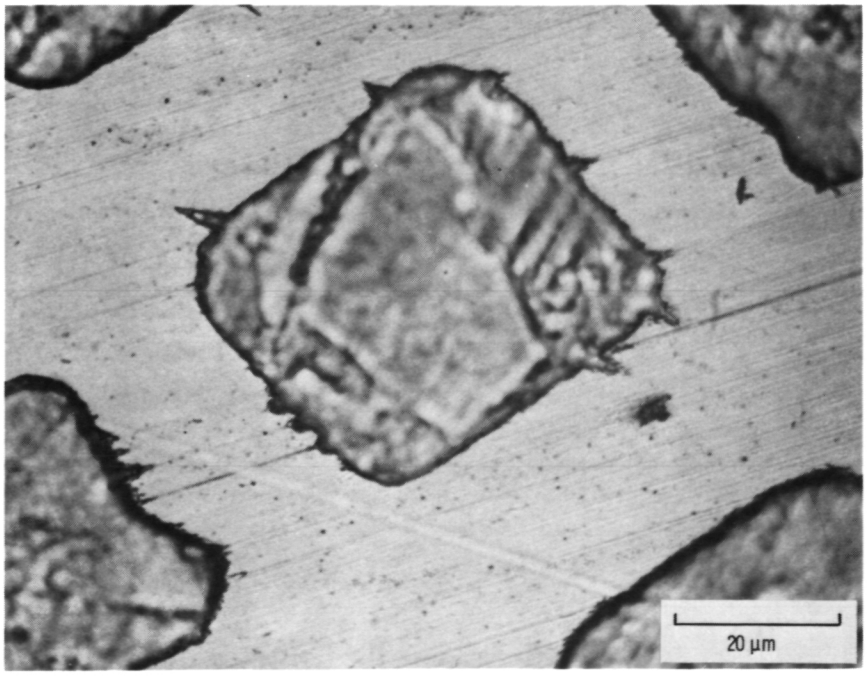

(b) Top view of an individual etched pit. The etched pits are approximately rectangular having mean lateral dimensions of 49 µm X 62 µm. The individual grains are visible at the bottom of the etched pits.

Figure 6.

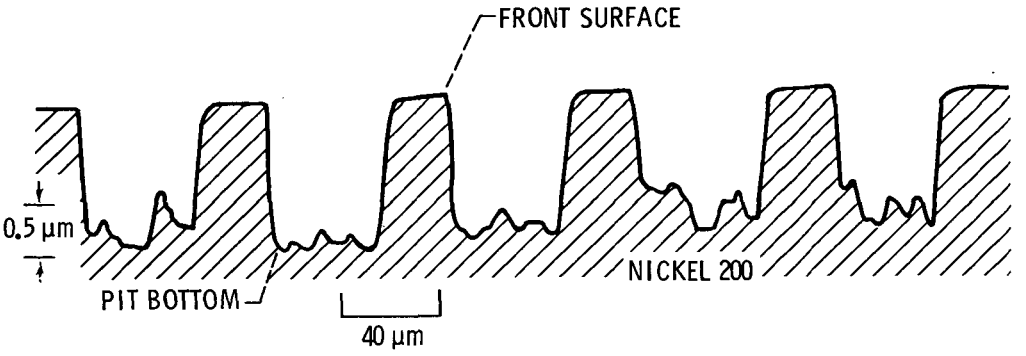

(c) Surface profile of the etched pits shown in (a) and (b).

Figure 6. - Concluded.

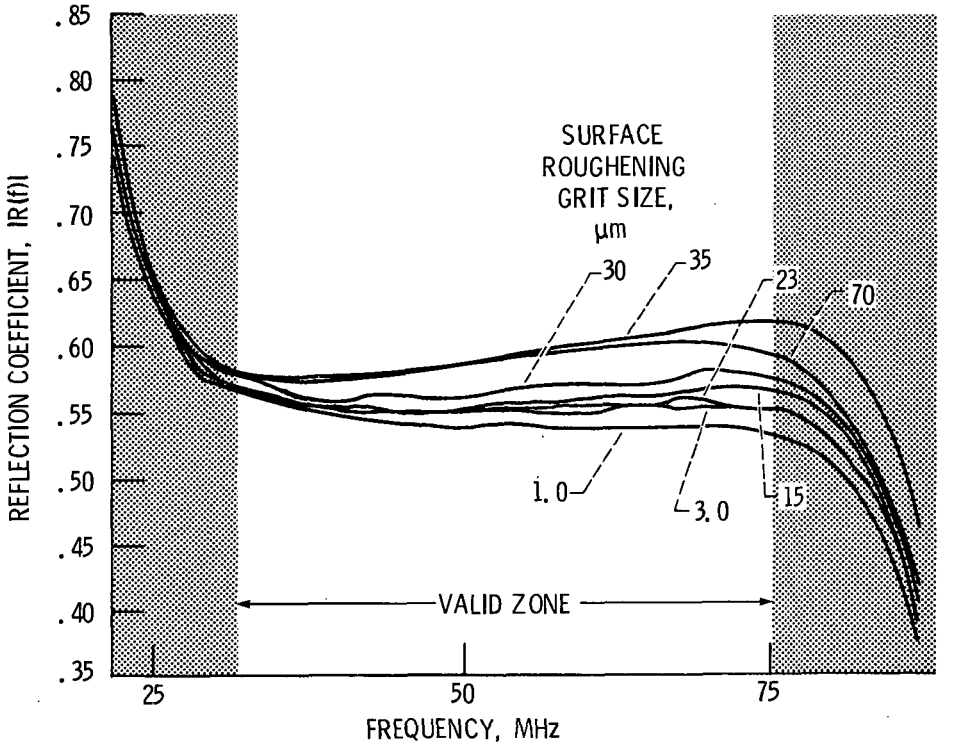

Figure 7. - Experimental reflection coefficient for varying surface roughness. The measured reflection coefficient (obtained by use of equation (1)). The numbers on the figure refer to the grit size used to roughen the surface of the nickel 200 sample. The valid frequency regime for comparing data lies in the unshaded area (as explained in the text).

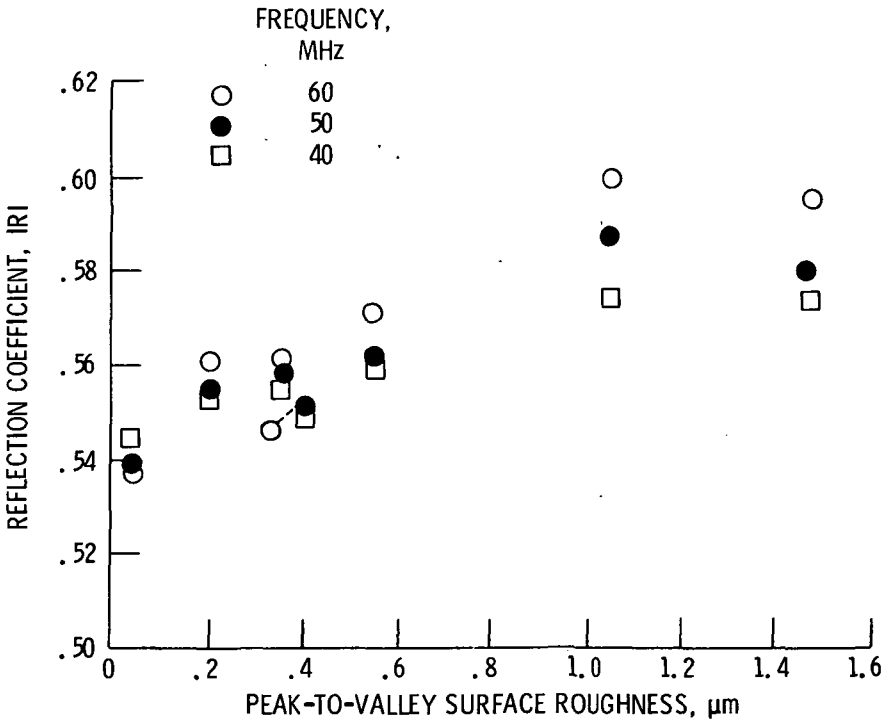

Figure 8. - Graph of measured reflection coefficient versus peak-to-valley roughness of the nickel 200 sample (see figs. 4 and 7). Data are shown for 40, 50, and 60 MHz.

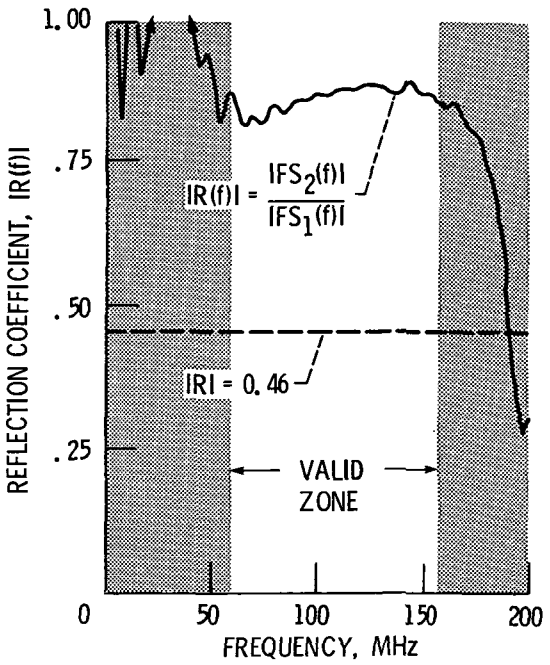

Figure 9. - The reflection coefficient for the ceramic MOR bar. The solid curve is the frequency dependent reflection coefficient determined by use of equation (1) and the dotted line is the constant reflection coefficient determined by use of equation (6).

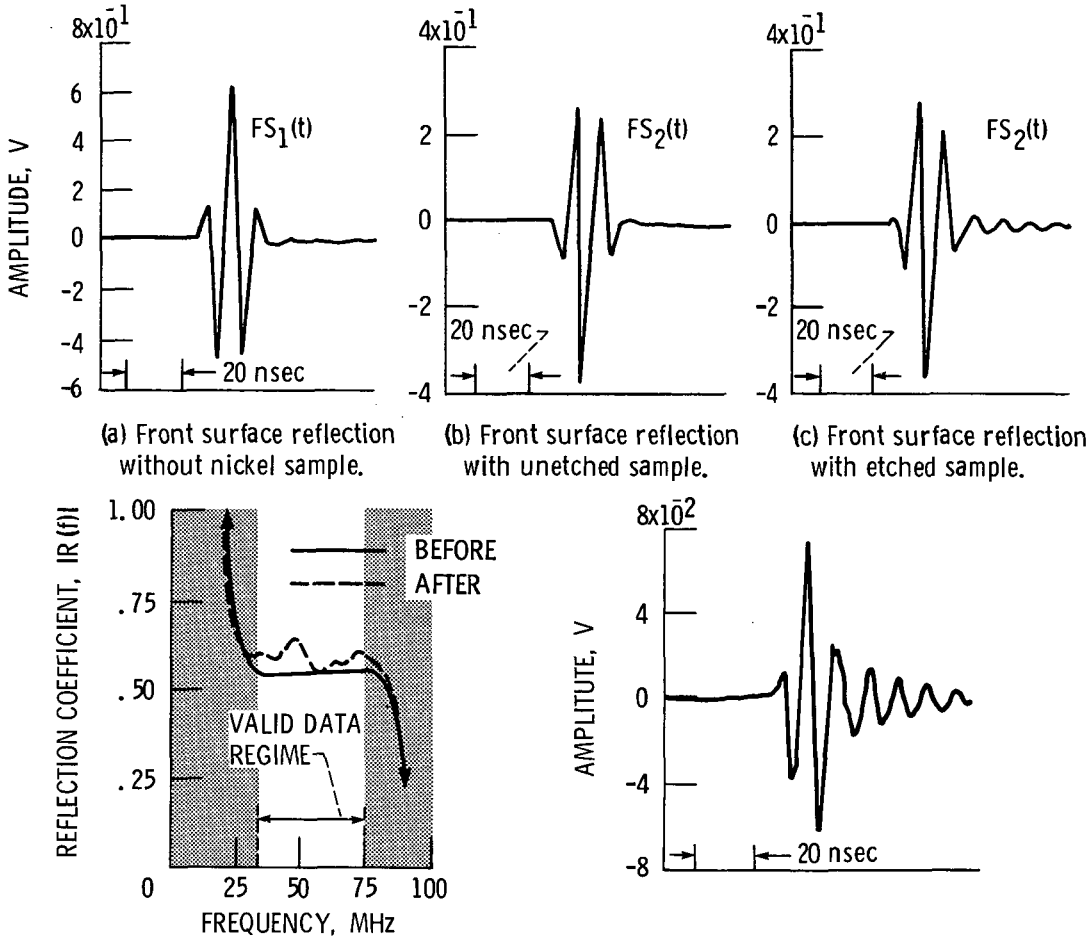

(a) Front surface reflection without nickel sample.

(b) Front surface reflection with unetched sample.

(c) Front surface reflection with etched sample.

(d) Reflection coefficient before and after etching.

(e) Residual reflected waveform obtained by subtracting the pulse shown in figure 10(b) from that shown in figure 10(c).

Figure 10. - Front surface reflection for nickel 200 sample before and after etching to produce surface with ordered, non-random scatters.

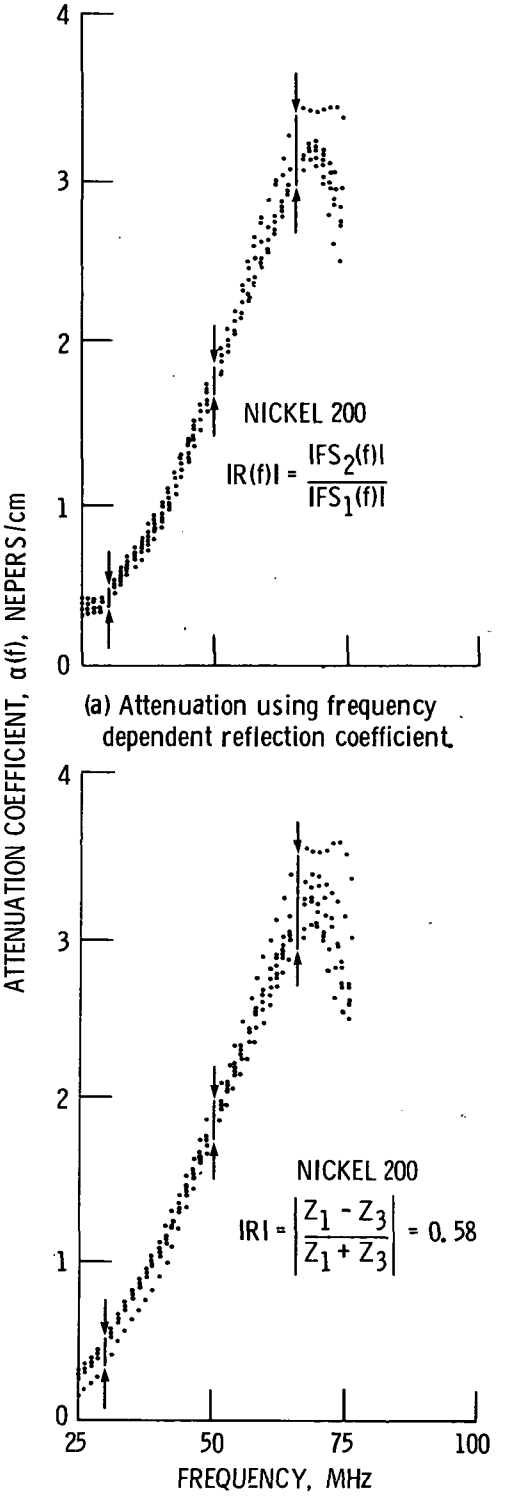

(a) Attenuation using frequency dependent reflection coefficient.

(b) Attenuation using frequency independent reflection coefficient.

Figure 11. - Attenuation coefficient for all surface roughnesses of the nickel 200 sample. In figure 11(a) attenuation coefficient was calculated using the reflection coefficient defined by equation 1. In figure 11(b) attenuation coefficient was calculated using equation (6).

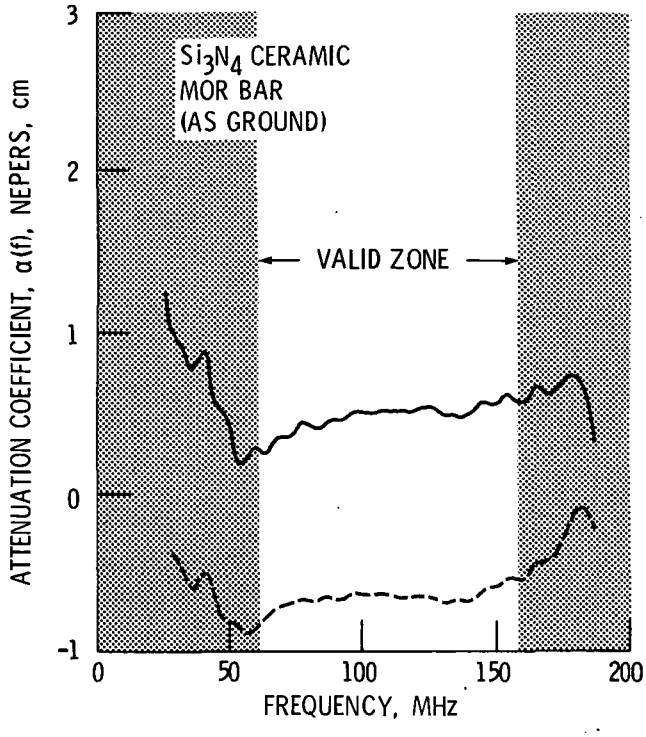

Figure 12. - The attenuation coefficient for the Si_3N_4 ceramic MOR bar. The solid curve is the for the case where the attenuation coefficient is determined using the frequency dependent reflection coefficient. The dotted curve is for the case where the attenuation coefficient is determined using the constant reflection coefficient.

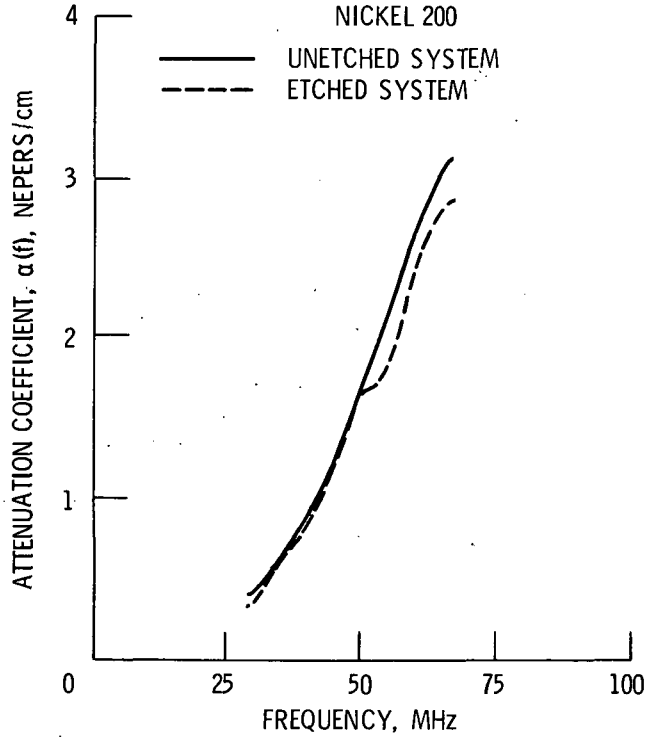

Figure 13. - The attenuation coefficient for the unetched and etched configuration is shown as solid and dotted curves, respectively.

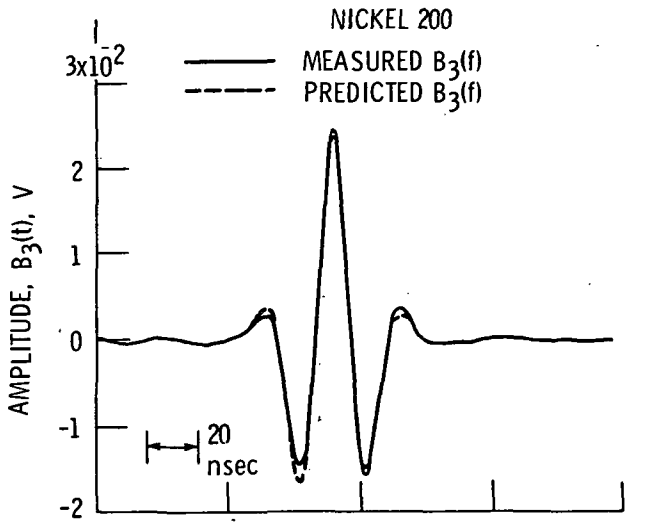

(a) Waveform.

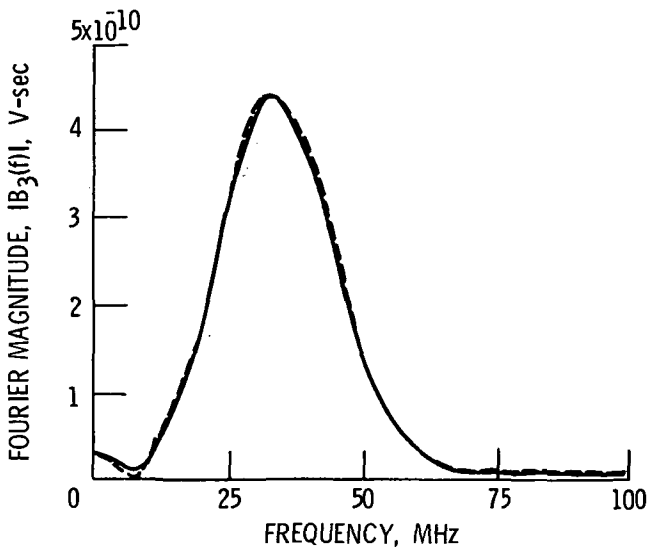

(b) Frequency spectra.

Figure 14. - Measured and predicted waveform and frequency spectra of echo B_3. The observed and predicted waveforms of pulse B_3 are shown in figure 14(a) as solid and dotted curves, respectively. Figure 14(b) shows the frequency spectra of the observed and predicted waveforms shown in figure 14(a). The observed and predicted magnitude spectra are shown as solid and dotted curves, respectively.

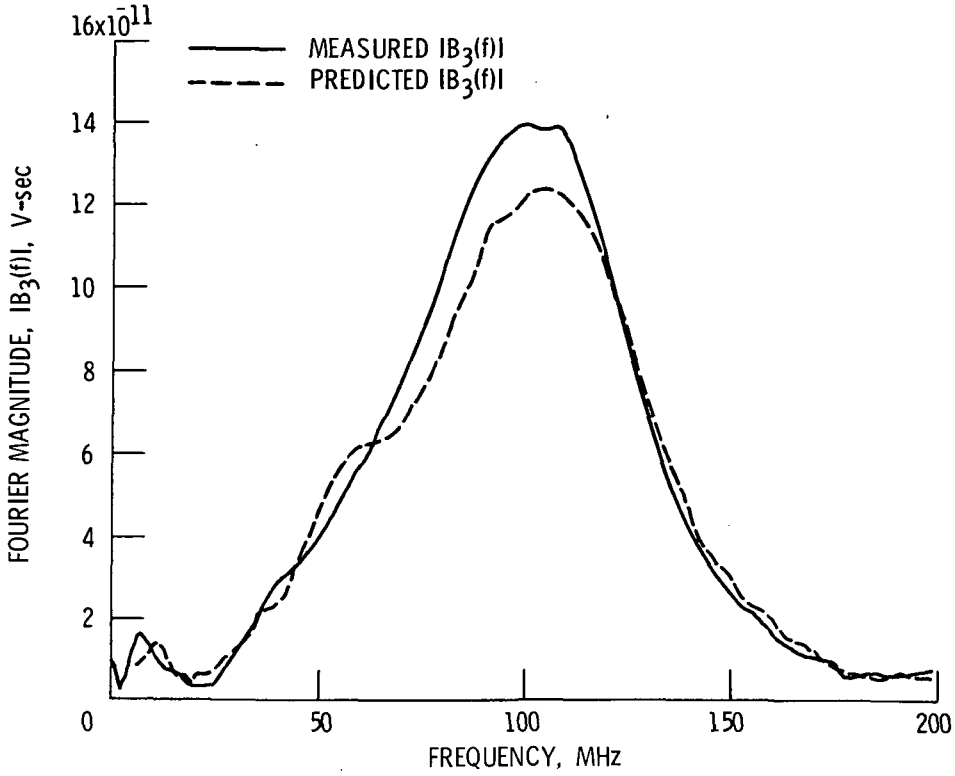

Figure 15. - Frequency spectra of pulse B_3 for the ceramic sample. The solid and dotted curves refer to the measured and predicted frequency spectra, respectively.

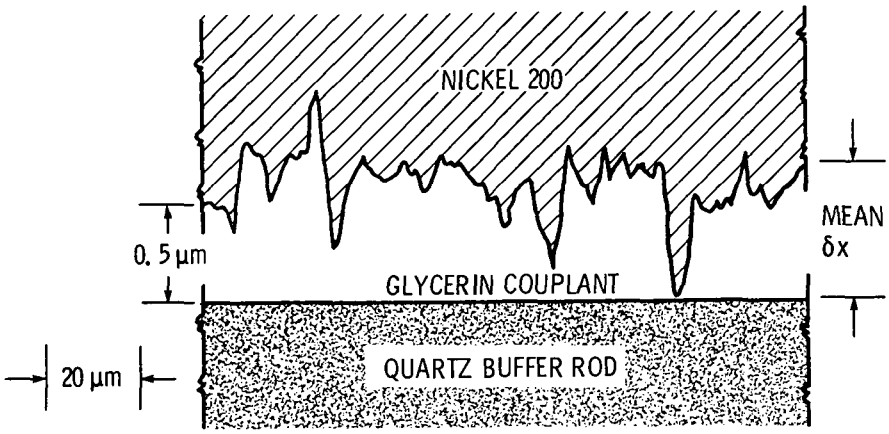

Figure 16. - Diagram of the effective mean couplant thickness δx. The surface roughness shown is that for the case of polishing with 35 μm silicon carbide grit.

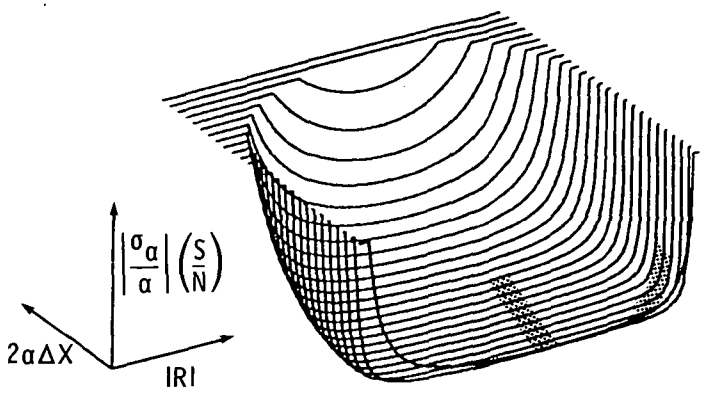

(a) Isometric projection of equation (9). The largest value of σ_α/α (S/N) shown is 10^3 and is indicated by flat regions at that value. The value of σ_α/α (S/N) in these flat regions, where σ_α/α (S/N) > 10^3, cannot be obtained from this figure but may be obtained by use of equation (9).

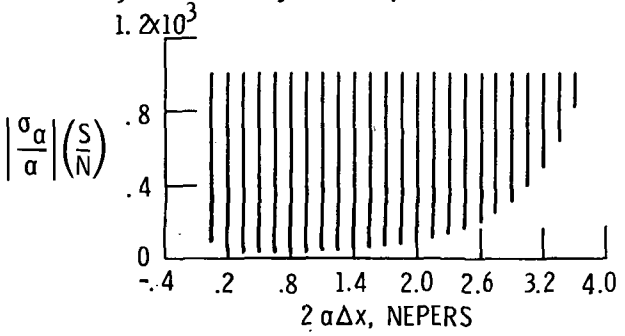

(b) Side view of figure 17(a).

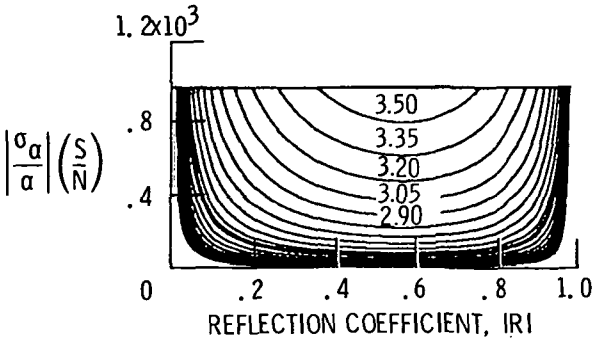

(c) Total loss ($2\alpha\Delta x$) by ultrasonic pulse in nepers during one round trip through sample. The plots shown in this figure are universal and are applicable to all systems that use the pulse-echo methodology described in the text.

Figure 17. - Isometric plot of variance due to uncertainty in pulse amplitude.

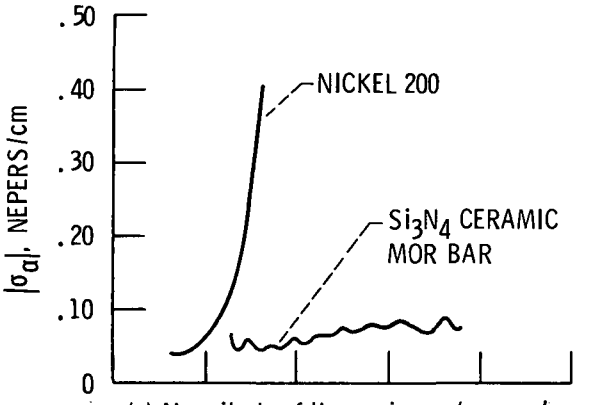

(a) Magnitude of the variance (nepers/cm) for the nickel 200 sample polished with 1.0-μm aluminum oxide and the as-ground Si_3N_4 ceramic MOR bar.

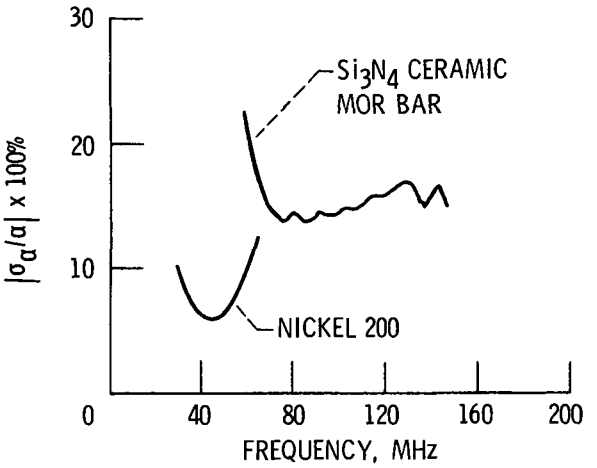

(b) Percent uncertainty in the measured attenuation coefficient for the nickel 200 sample polished with 240-grit silicon carbide and the as-ground Si_3N_4 ceramic MOR bar.

Figure 18. - Variance of the attenuation measurement.

1. Report No.	2. Government Accession No.	3. Recipient's Catalog No.
NASA TM-83788		

4. Title and Subtitle	5. Report Date
The Role of the Reflection Coefficient in Precision Measurement of Ultrasonic Attenuation	6. Performing Organization Code 505-53-1A
7. Author(s)	8. Performing Organization Report No. E-2185
Edward R. Generazio	10. Work Unit No.
9. Performing Organization Name and Address National Aeronautics and Space Administration Lewis Research Center Cleveland, Ohio 44135	11. Contract or Grant No.
12. Sponsoring Agency Name and Address National Aeronautics and Space Administration Washington, D.C. 20546	13. Type of Report and Period Covered Technical Memorandum 14. Sponsoring Agency Code

15. Supplementary Notes

Prepared for the 1984 Annual Review of Progress in Quantitative Nondestructive Evaluation sponsored by the Defense Advanced Research Projects Agency (DARPA), LaJolla, California, July 8-13, 1984.

16. Abstract

Ultrasonic attenuation measurements using contact, pulse-echo techniques are sensitive to surface roughness and couplant thickness variations. This can produce considerable inaccuracies in the measurement of the attenuation coefficient for broadband pulses. Inaccuracies can arise from variations in the reflection coefficient at the buffer-couplant-sample interface. In this paper, the reflection coefficient is examined as a function of the surface roughness and corresponding couplant thickness variations. Interrelations with ultrasonic frequency are illustrated. It is shown that reliable attenuation measurements are obtained only when the frequency dependence of the reflection coefficient is incorporated in signal analysis. Data are given for nickel 200 samples and a silicon nitride ceramic bar having surface roughness variations in the 0.3 to 3.0 μm range for signal bandwidths in the 50 to 100 MHz range.

17. Key Words (Suggested by Author(s))	18. Distribution Statement
Attenuation; Ultrasonics; Ultrasonic attenuation; Reflection coefficient; Surface roughness; Surface topology; Nondestructive testing; Nondestructive evaluation	Unclassified - unlimited STAR Category 38

19. Security Classif. (of this report)	20. Security Classif. (of this page)	21. No. of pages	22. Price*
Unclassified	Unclassified		

*For sale by the National Technical Information Service, Springfield, Virginia 22161

National Aeronautics and
Space Administration

Washington, D.C.
20546

Official Business
Penalty for Private Use, $300

SPECIAL FOURTH CLASS MAIL
BOOK

Postage and Fees Paid
National Aeronautics and
Space Administration
NASA-451

NASA

POSTMASTER: If Undeliverable (Section 158
Postal Manual) Do Not Return